Fault Diagnostics for Electrically Operated Pitch Systems in Offshore Wind Turbines

Fault Diagnostics for Electrically Operated Pitch Systems in Offshore Wind Turbines

Surya Teja Kandukuri[1], Van Khang Huynh[2], Hamid Reza Karimi[3], Kjell Gunnar Robbersmyr[4]

[1,2,4]Department of Engineering Sciences, University of Agder, Grimstad, Norway
[3]Department of Mechanical Engineering, Politecnico di Milano, Milan, Italy

E-mail: [1]suryak@uia.no, [2]huynh.khang@uia.no, [3]hamidreza.karimi@polimi.it, [4]kjell.g.robbersmyr@uia.no

Abstract. This paper investigates the electrically operated pitch systems of offshore wind turbines for online condition monitoring and health assessment. The current signature based fault diagnostics is developed for electrically operated pitch systems using model-based approach. The electrical motor faults are firstly modelled based on modified winding function theory and then, current signature analysis is performed to detect the faults. Further, in order to verify the fault diagnostics capabilities in realistic conditions, the operating profiles are obtained from FAST simulation of offshore wind turbines in various wind conditions. In this way, the applicability of current signature analysis for fault diagnostics in offshore wind turbine pitch systems is demonstrated.

1. Introduction

Offshore wind is among promising renewable energy industries growing at a rapid pace. Although offshore wind farms are advantageous, it has been witnessed that their maintenance costs are high and reliability is low compared to their onshore counterparts. This is due to the harsh weather conditions and limited weather windows for performing maintenance activities. As the offshore wind farms grow larger and further offshore, it becomes imperative to adopt a maintenance strategy in order to operate them reliably and profitably [1]. Condition monitoring and condition based maintenance are necessary tasks in realising such maintenance strategy. In so far, the condition monitoring systems (CMS), that are commercially available, are focused primarily on the drivetrain, generator, main bearing and blades [2]. Upgrading the maintenance method to condition based maintenance at component level can enhance such a maintenance strategy. Towards this end, the electrically operated pitch systems in offshore wind turbines are assessed for condition based maintenance.

The pitch system in a wind turbine operates intermittently, depending on the wind conditions in order to reduce structural loads and improve the turbine efficiency. These are either hydraulically or electrically actuated. It is estimated that the market is equally split between the two types of actuation [3]. In this paper, the electrically operated pitch systems are studied. An electrically operated pitch system consists of a multi-stage planetary gearbox with an electric motor as prime-mover. The gearbox drives the blade bearing (a large slew bearing) through a pinion. The bearing has a gear on the inner perimeter of the inner ring and the blade is bolted to the inner ring. The outer ring is rigidly bolted to the hub. Due to this arrangement, the blade root

loads are transferred to the blade bearing. The pitch system therefore experiences the periodic gravitational loads and aperiodic wind disturbance and gyroscopic loads that result in wide variations in operating profiles, which could lead to failures in the motor, gearbox and blade bearing.

The pitch systems have been reported among the wind turbine components with frequent failures [4]. There has been great attention in the literature on the control problem of the pitching mechanism [5], pitch actuator fault tolerance [6] and fault detection [7]. However, to the authors' knowledge, there are little published efforts that are focused on predictive maintenance approach for pitch systems. A predictive maintenance approach should include incipient fault diagnosis, fault severity assessment and remaining useful life estimation so that a maintenance action may be planned. For instance, detecting a bearing fault before it jams the pitch actuator, can help in maintenance planning. It can be understood that the health monitoring of pitch drive mechanisms has been a low priority because of the fact that they are easily replaceable in onshore turbines. However, the need for such predictive maintenance of these systems is becoming stronger in case of offshore as such reactive maintenance measures are expensive, owing to the cost of transportation and weather conditions.

In this article, the main objective is to determine the feasibility and applicability of current signature analysis for pitch motors in typical operating profiles. In order to determine pitch system operation profiles, the 5MW reference wind turbine is simulated in FAST analysis tools developed by National Renewable Energy Laboratory (NREL) [8]. The pitch systems however pose significant challenge in terms of intermittent, start-stop operating profiles and low speed operations. The main contribution of this paper is therefore twofold: 1) to develop a detailed physical modelling of various motor faults and study their effect on motor currents in pitch system operating profiles; and 2) to determine the feasibility of current signature analysis in such operating profiles.

The rest of this paper is organised as follows: In Section 2, determination of the typical pitch profiles from FAST analysis tool is described. Further, a detailed modelling of induction motor with implementation of various fault conditions is described in Section 3. In Section 4, the motor current signature analysis is tested for pitch motor diagnostics in various wind turbine operating profiles. Finally, accuracy of the fault detection algorithms and steps towards implementation in wind farms are discussed.

2. FAST analysis

The wind turbine blade root loads are studied based on FAST analysis tool. Various full-field wind conditions and wave conditions are generated using TURBSIM software for simulation purposes [9]. The 5 MW reference wind turbine is then simulated to determine the command pitch angles based on GH-Bladed dll style controller [8]. In order to gain insight into the pitch system operation, the specifications of the pitch motor, gearbox and blade bearing are required for simulation study. However, this information is not generic and vary with turbine model. The selected reference wind turbine uses blade structure definition based on LM Glasfibers LM64-5 blade, with a reduced length of 61.2m. The bolt circle diameter for a 61.2m long blade LM-61.2P is obtained from the LM Wind Powers website as 2.3m [10]. A 4-point contact bearing KD-320 series, with inner ring gear and inner bolt circle diameter of 2.43m is chosen from Rothe Erde Thyssen Krupp slew bearings catalog [11], which is designed to withstand a simultaneous axial loads of up to 3600kN and moment load of 2600kNm. The inner race gear has 144 gear teeth.The pitch drive is required to generate torque equal to the rotating torque of the slew bearing. The starting torque of the slew bearing is given by semi-empirical relationship [11] as

$$T_{start} = \frac{\mu}{2}(4.4M_k + F_a D_l + 2.2(F_r D_l)) \quad (1)$$

where F_a is the axial load (kN), F_r is the radial load (kN), M_k is the resultant tilting moment (kNm), D_l is the bearing race diameter (m) and $\mu = 0.004$ is the coefficient of friction of the bearing. These axial and radial loads are the blade-root forces and moments obtained from the FAST simulation. Although, in reality the rolling torque of the bearing is much lesser than T_{start}, it is complex to calculate as it depends on factors such as elasto-hydrodynamics of lubrication, bearing-seal friction and contact mechanics [12]. Therefore, T_{start} is assumed as the resultant bearing torque that is to be counteracted by the pitch drive. This is a conservative but acceptable assumption as the objective here is not to design a pitch bearing but to evaluate feasibility of diagnostics.

Further, a multistage planetary gearbox RPR255FA from Brevini [13] is chosen with a gear ratio of $1 : 322.9$. The connecting pinion gear has 14 teeth. Finally, a two-pole induction motor is chosen as the prime-mover. The FAST simulation presently, does not include pitch actuator dynamics. These are typically approximated by a second-order system [14] as

$$\begin{aligned} \dot{x}_p &= \begin{bmatrix} -2\omega_n\eta & -\omega_n^2 \\ 1 & 0 \end{bmatrix} x_p + \begin{bmatrix} 1 \\ 0 \end{bmatrix} u_p \\ y_p &= \begin{bmatrix} 1 & 0 \\ 0 & \omega_n^2 \end{bmatrix} x_p \end{aligned} \tag{2}$$

where the natural frequency is $\omega_n = 0.88$ rad/s and the damping ratio is $\eta = 0.9$. The state vector x_p has the velocity and position of the pitch actuation and u_p has the pitch actuator command obtained from FAST. Under normal operations (apart from emergency shutdown), the pitch rate is limited to $\pm 5^o$/s and the acceleration to $\pm 30^o/\text{s}^2$.

The 5 MW reference wind turbine is simulated in offshore monopile configuration with a turbulent full-field wind profile generated by TurbSim. The Kaimal spectrum is simulated with a mean wind speed of 18 m/s and turbulence class A, as per IEC standards [15]. The wave profile is selected with a significant wave height $H_s = 6$ m and the time period of $T_p = 10$ seconds. The resultant pitch angle, speed profile and maximum starting torque at the bearing are described in Figure 1. It can be seen that for most part of the operating period, the motor runs at very low speeds, lesser than 1000 rpm while the loads are continuously varying. The objective is therefore, to verify the detectability of current signatures in such operating conditions.

3. Induction motor behaviour in faulty conditions

The induction motors are common prime movers in many industrial scenario as they are inexpensive and robustly built to withstand a wide range of operating and environmental conditions. A three-phase induction motor typically consists of sinusoidally distributed stator windings and a squirrel cage rotor with a number of rotor bars that are shorted at both ends with end rings. It was observed that bearing faults contribute to 41% of the total failures, while stator turn faults contribute to 37%, rotor related failures 10% [16]. In this paper the behaviour of induction motor is studied under all of the aforementioned fault conditions in closed-loop under pitch system operating conditions.

The concept of motor current signature analysis (MCSA) is well-established in literature, see for instance [17] and [18]. The principal idea in MCSA is that the mechanical faults inside an electrical motor tend to disturb the air gap, leading to a periodic variation in the magnetic field as the rotor rotates. Similarly, the electrical faults such as the stator winding or rotor-bar faults result in changes in electrical circuit.These variations in turn, affect the stator current and can be detected in the Fourier spectrum of single line current at specific frequencies.

The motor is typically modelled using dq-modelling approach [19] with rotor represented by a fictitious lumped winding for performance analysis and control design. In order to study the behaviour of induction motor in faulty conditions, a detailed model based on modified winding

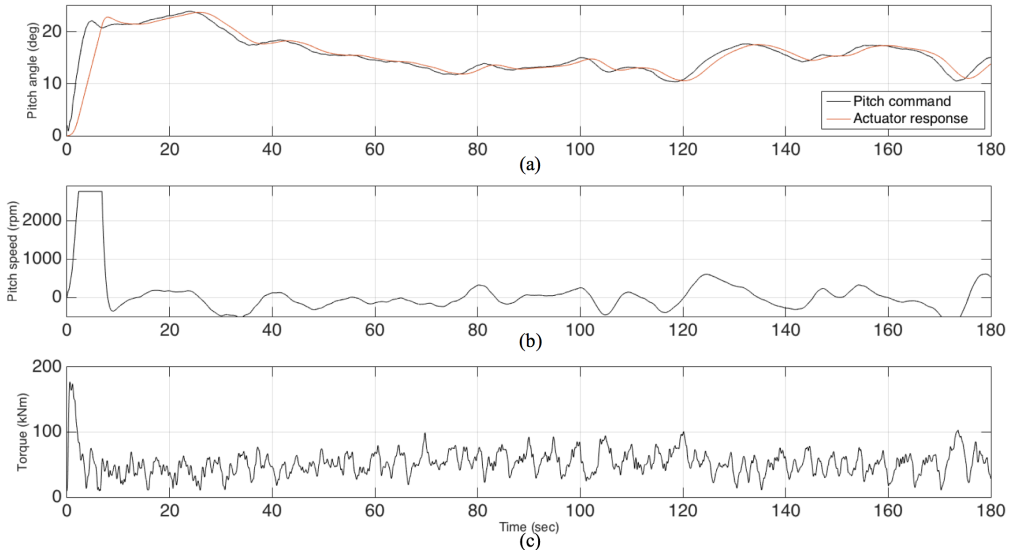

Figure 1. Time response of pitch angle (a), pitch motor speed (b) and bearing torque (c)

function theory (MWFTh) has been utilised. This modelling approach provides the ability to incorporate the electrical and mechanical faults into the model and analyse the faulty behaviour. This gives insight into the effect of various factors on the capability of MCSA such as the severity of fault on the machine behaviour, the behaviour of faulty machines in closed loop, varying speeds and varying load conditions. All of these are necessary considerations for diagnostics in wind turbine pitch systems.

The electrical circuit of the induction motor is rewritten by considering all magnetic interactions between each stator winding and rotor bar through the machine airgap. Based on the winding function theory [20], the mutual inductance between two stator windings corresponding to phases A and B can be expressed as

$$L_{AB} = \frac{\mu_0 r l}{g} \int_0^{2\pi} N_A(\phi,\theta) N_B(\phi,\theta) d\phi \tag{3}$$

where N_A represents the winding function of the phase A winding and N_B represents that of phase B. The ϕ represents the spatial angle inside the machine and θ represents the rotor position. μ_0 represents the permissivity of air, r is the radius of the rotor, l is the effective length of rotor and g is the length of airgap.

In case of the sinusoidally distributed stator windings, the winding function for phase A of the rotor is given by:

$$N_A(\phi,\theta) = \frac{N_s}{p} cos\phi \tag{4}$$

where N_s is the number of stator winding turns per phase and p is the number of pole pairs. The winding functions for the phases B and C lag phase A by 120^o and 240^o, respectively. The rotor bar winding function is given by:

$$N_i(\phi,\theta) = \begin{cases} -\frac{\alpha_r}{2\pi} & 0 \le \phi < \theta_i \\ 1 - \frac{\alpha_r}{2\pi} & \theta_i \le \phi < \theta_{i+1} \\ -\frac{\alpha_r}{2\pi} & \theta_{i+1} \le \phi < 2\pi \end{cases} \tag{5}$$

where $i \in N_r$, the number of rotor bars and $\theta_i = \theta + (i-1)\alpha_r$ and $\alpha_r = 2\pi/Nr$.
The induction motor dynamics can be represented by the equations

$$\begin{aligned} \{V_s\}_{(3\times1)} &= [R_s]_{(3\times3)}\{i_s\}_{(3\times1)} + \tfrac{d}{dt}\left([L_s]_{(3\times3)}\{i_s\}_{(3\times1)} + [L_{sr}]_{3\times N_r}\{i_r\}_{N_r\times1}\right) \\ \{0\}_{(N_r\times1)} &= [R_r]_{(N_r\times N_r)}\{i_r\}_{(N_r\times1)} + \tfrac{d}{dt}\left([L_r]_{(N_r\times N_r)}\{i_r\}_{(N_r\times1)} + [L_{rs}]_{N_r\times3}\{i_s\}_{3\times1}\right) \end{aligned} \tag{6}$$

where V_s represents the three-phase power supply, i_s is the stator current, i_r represents the rotor bar currents in N_r bars, R_s is the stator resistance of the three phase windings and R_r represents the individual rotor bar resistance. The self and mutual inductances of stator windings are captured in L_s and L_r, respectively, while the mutual inductance between each stator winding and rotor bar are captured in L_{sr} and $L_{rs} = L_{sr}^{'}$.
Further, the mutual inductance L_{sr} is variable with respect to the rotor angular displacement θ_r, therefore

$$\frac{d}{dt}(L_{sr}i_r) = \frac{p}{2}\omega_r\frac{\partial L_{sr}}{\partial\theta_r}i_r + L_{sr}\frac{di_r}{dt} \tag{7}$$

The rotor electromechanical torque is given by:

$$T_{em} = \frac{p}{2}i_s^{'}\frac{\partial L_{sr}}{\partial\theta_r}i_r \tag{8}$$

and the angular speed and angular displacement of the rotor are given by:

$$\begin{aligned} \tfrac{d\omega_r}{dt} &= \tfrac{p}{2J}(T_{em} - T_l) \\ \tfrac{d\theta_r}{dt} &= \omega_r \end{aligned} \tag{9}$$

T_l is the external mechanical load on the rotor.
Now one may write the state space of the electrical motor of the form $A_1\dot{x}(t) = A_2x(t) + u(t)$
where

$$x(t) = \left\{ \begin{array}{cccc} i_s & i_r & \omega_r & \theta_r \end{array} \right\}' \tag{10}$$

and the input vector $u(t)$ is given by:

$$u(t) = \left\{ \begin{array}{cccc} v_s & 0_{N_r} & \frac{p}{2J}(T_{em} - T_l) & 0 \end{array} \right\}' \tag{11}$$

with the matrices

$$A_1 = \begin{bmatrix} L_s & L_{sr} & 0 & 0 \\ L_{rs} & L_r & 0 & 0 \\ 0 & 0 & 1 & 0 \\ 0 & 0 & 0 & 1 \end{bmatrix}$$

$$A_2 = \begin{bmatrix} -R_s & -\omega_r\frac{\partial L_{sr}}{\partial\theta_r} & 0 & 0 \\ -\omega_r\frac{\partial L_{rs}}{\partial\theta_r} & -R_r & 0 & 0 \\ 0 & 0 & 0 & 0 \\ 0 & 0 & 1 & 0 \end{bmatrix} \tag{12}$$

The dynamic model of induction motor based on winding function theory is thereby developed in the manner as described in [21]. In case of mechanical faults, such as airgap eccentricity or

a bearing fault, the airgap g is no longer constant. The mutual inductance is now based on *modified* winding function [22] given by:

$$L_{AB} = \mu_0 rl \left[\int_0^{2\pi} n_A(\phi,\theta) n_B(\phi,\theta) g^{-1}(\phi,\theta) d\phi - 2\pi < M_A(\phi,\theta) >< M_B(\phi,\theta) >< g^{-1}(\phi,\theta) > \right] \tag{13}$$

where $M_i(\phi,\theta)$ represents the corresponding modified winding function of the winding 'i' and $< M_i(\phi,\theta) >$ represents its mean value described as follows:

$$< M_i(\phi,\theta) >= \frac{1}{2\pi < g^{-1}(\phi,\theta) >} \int_0^{2\pi} n_i(\phi,\theta) g^{-1}(\phi,\theta) d\phi \tag{14}$$

In case of a dynamic airgap eccentricity (AGE) fault, such as with unbalanced load or bent shaft, the airgap varies spatially, depending on the speed of rotation. Thus the new airgap is defined as [23]

$$g^{-1}(\phi,\theta) = \frac{1}{g(1 - e\ cos(\phi - \theta))} \tag{15}$$

where e is a tunable parameter to approximate the degree of severity of the fault. In case of a bearing fault [24], the airgap function varies periodically, whenever the rolling element passes the crack on the bearing outer ring. This is approximated by a series of Dirac delta functions as

$$g^{-1}(\phi,\theta) = \left[g(1 - e\ cos(\phi - \theta) \sum_{k=-\infty}^{\infty} \delta(t - \frac{k}{f_c})) \right]^{-1} \tag{16}$$

where f_c is the corresponding fault frequency for inner race, outer race and rolling element faults. In case of electrical faults, such as the broken rotor bar fault (BRB), the bars crack and their resistance increases largely compared to the healthy bars. As the bars are not insulated from the rotor in low power induction motors, the circuit does not break completely [22]. Therefore, the BRB fault can be simulated by merely increasing the resistance of rotor bars. In case of a stator-turn fault (STF), the shorted windings form an additional stator winding loop. For instance, if the stator winding of phase A has shorted coils, these coils form a separate circuit with fault current flowing through it. If the winding A has a percentage of windings that are shorted, the inductance and resistance of coil A are proportionally decreased and its mutual inductances with other stator windings as well as rotor-bars are recalculated accordingly. The stator now has 4 windings instead of 3 and the system of equations (6) can be represented as:

$$\begin{aligned} \{V_s\}_{(4\times1)} &= [R_s]_{(4\times4)}\{i_s\}_{(4\times1)} + \tfrac{d}{dt}\left([L_s]_{(4\times4)}\{i_s\}_{(4\times1)} + [L_{sr}]_{4\times N_r}\{i_r\}_{N_r\times1}\right) \\ \{0\}_{(N_r\times1)} &= [R_r]_{(N_r\times N_r)}\{i_r\}_{(N_r\times1)} + \tfrac{d}{dt}\left([L_r]_{(N_r\times N_r)}\{i_r\}_{(N_r\times1)} + [L_{rs}]_{N_r\times4}\{i_s\}_{4\times1}\right) \end{aligned} \tag{17}$$

For the cases of AGE and BRB, the self and mutual inductance matrices L_s, L_r and L_{sr} are recalculated as described in the equation (13). Notice that in case of AGE and BRB faults, the inductances are calculated at every time step as they vary based on the rotor angular position. The induction motor is thus simulated in various faulty conditions in a similar fashion as described in [21, 25].

A 4 kW three-phase two-pole, 220 V star connected induction motor is simulated in all the different fault cases described, the parameters of the motor are specified in Appendix-A. The motor is started at no-load and then a load of 8 Nm is added after 1.2 seconds. The stator phase A current is then analysed through Fast Fourier transform (FFT).

In case of healthy motor, directly fed from the mains with a steady, balanced 220 V supply,

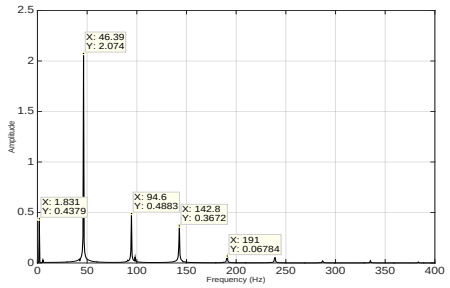

Figure 2. Fault frequencies at f_{AGE_1}

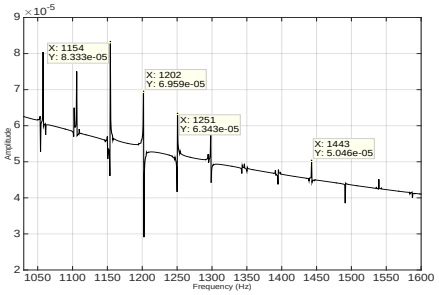

Figure 3. Fault frequencies at f_{AGE_2}

the Fourier spectrum of the current shows only one peak at the supply frequency 50 Hz. As this is a simulation, the motor is assumed to be perfectly healthy, without any manufacturing defects. In case of the AGE fault, it has been noticed that the presence of spectral components corresponding to the fault increase in magnitude with increase in degree of eccentricity[26]. Two different fault harmonics are seen in Fourier spectrum, one near the supply frequency given by:

$$f_{AGE_1} = |f_s \pm k f_{rot}|, \quad k = 1, 2, 3 \ldots \tag{18}$$

and another at the principal slot harmonic given by

$$f_{AGE_2} = \left[\frac{(kN_r \pm n_d)(1-s)}{p} \pm 1 \right], \quad n_d = 1, 2, 3 \ldots \tag{19}$$

where f_s is the supply frequency, f_{rot} is the rotor frequency in Hz, s is the slip and p is the number of pole-pairs in the motor. These are depicted in Figures 2 and 3. It is to be noted that the ratio of number of poles to the rotor bars plays a significant role in the detectability of AGE fault in an induction motor [27]. The higher frequency harmonics, especially f_{AGE_2} depend on this ratio. It was noticed that the same motor with 39 rotor bars instead of 28, has shown significantly better magnitude of the fault signatures in the current spectrum. However, the f_{AGE_1} was certainly detectable in all cases. Besides, the fault magnitudes increase with increase in degree of severity e and the load as well. The fault signatures are significantly higher in magnitude with loads closer to the rated loads.

The broken rotor bar fault increases with an increase in number of broken rotor bars and severity of fault. For instance, in Figure 4, the current spectrum corresponding to two broken rotor bars is shown. The supply frequency $f_s = 50$ Hz is filtered using a notch filter. The resistance of the two bars was increased by 50 times the normal resistance and the fault frequencies appear at

$$f_{BRB} = |f_s(1 \pm 2s)| \tag{20}$$

The faults increase in magnitude with an increase in bar resistance or load. It was noticed that the fault is undetectable at no-load, understandably so, because there will be almost no induced current in the rotor bars at negligible slip.

Bearing faults in case of bearings on the rotor shafts are more likely to be outer race faults due to the fact that the centrifugal forces are always directed outwards as the shaft is rotating and the outer race is rigidly fixed. Therefore, only outer race fault is simulated and it can be seen that the bearing fault frequencies are detected in the single phase current spectrum as described by:

$$f_{BRG} = |f_s \pm k f_c|, \quad k = 1, 2, 3 \ldots \tag{21}$$

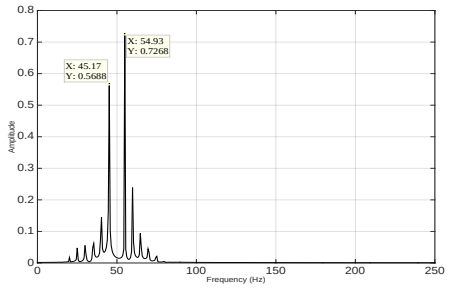

Figure 4. Broken rotor-bar fault spectrum

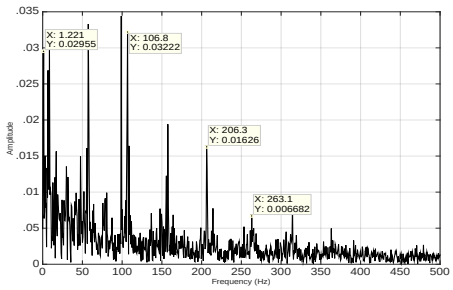

Figure 5. Bearing fault spectrum

where f_c is the outer raceway fault frequency given by:

$$f_c \approx 0.4 N_b f_{rot} \tag{22}$$

for 6 to 12 rolling elements[28], where N_b is the number of rolling elements in the bearing. It was noticed that the bearing fault frequencies increase in magnitude with increase in degree of severity e. Besides, with increase in load, the spectrum shows increase in spectral content across the frequencies and decreases the detectability of fault signature. The bearing fault signature at 5 Nm load is shown in Figure 5.

In case of the stator-turn faults, the single phase current spectrum did not show the fault at the principal slot harmonics as described in [29]. However, it was observed that the extended Park's vector analysis (EPVA) has shown promising results [30]. The dq-current components according to EPVA are described by:

$$\begin{aligned} i_d &= \sqrt{\tfrac{2}{3}} i_A - \sqrt{\tfrac{1}{6}} i_B - \sqrt{\tfrac{1}{6}} i_C \\ i_q &= \sqrt{\tfrac{1}{2}} i_B - \sqrt{\tfrac{1}{2}} i_C \end{aligned} \tag{23}$$

The i_d and i_q currents have shown a fault component at $3f_s$ that increases with increase in fault magnitude and not at $2f_s$, as described in [30]. Besides, as described in [31], the loci of the plot (i_d, i_q) is circular in case of healthy machine and takes an elliptical pattern in case of the stator winding faults. The stator winding faults signature at $3f_s$ and the ellipticity of dq loci increase with increase in the number of faulty windings. However, it was noticed that load has understandably, little effect on the fault signature. These results were described in the Figure 6 and 7. The frequency signatures as calculated by the formulae for AGE, BRB, BRG described by equations (18-21) are shown in Table 1, which show good agreement with the frequency spectrum obtained from simulation of faulty models.

Insofar, all the described faults of induction motor are physically simulated at supply frequency and the effect of fault severity and variation of load are studied. However, in pitch systems, the motor operates in closed loop with a controller and runs at lower speeds with heavy loads. Further, the closed loop behaviour of the induction motor shall be evaluated.

4. Faulty machine behaviour in closed loop

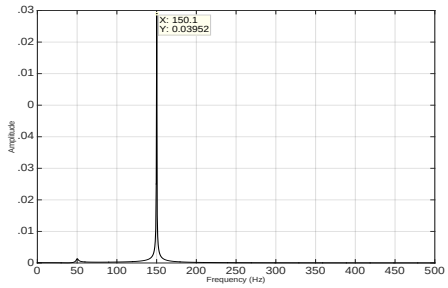

Figure 6. i_d current spectrum

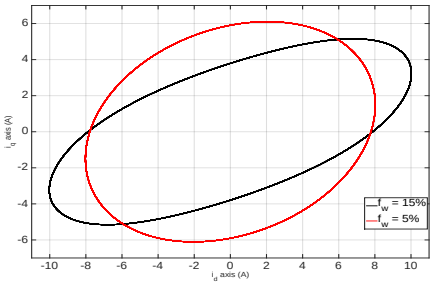

Figure 7. dq-current loci

Table 1. Calculated fault frequencies in open-loop

f_{BRG}(Hz)	f_{BRB}(Hz)	f_{age_1}(Hz)	f_{age_2}(Hz)
106.5	54.92	94.47	1250.3
206.5	45.07	1.84	1154
263		142.63	1202
		46.32	1302

In order to simulate pitch operations, vector control for induction motors has been adopted as the control strategy as described in Figure 9. An inverse half-Γ model of induction motor, as described in Figure 8, is developed as it is suitable for control applications. The necessary parameters for this model are derived based on the physical parameters of the induction motor as described in Appendix-A. The system of equations representing the dynamics of the lumped model in stator coordinates are

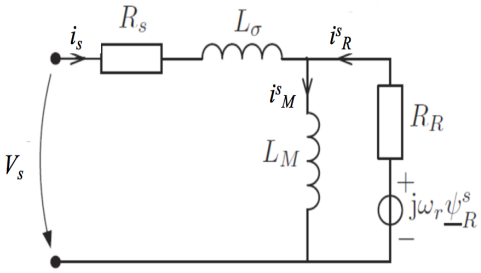

Figure 8. Inverse half-Γ model

$$\{V_s\}_{(3\times1)} = [R_s]_{(3\times3)}\{i_s\}_{(3\times1)} + \frac{d}{dt}\{\psi^s_s\}_{(3\times1)}$$

$$0_{(3\times1)} = [R_R]_{(3\times3)}\{i^s_R\}_{(3\times1)} + \frac{d}{dt}\{\psi^s_R\}_{(3\times1)} - j\omega_r\{\psi^s_R\}_{(3\times1)} \tag{24}$$

where $\psi^s_s = L_\sigma i^s_s + L_M i^s_M$, $\psi^s_R = L_M i^s_M$, $L_M = L^2_m/Lr$, $L_\sigma = L_s - L_M$, $R_R = (L_m/L_r)^2 Rr$, $L_s = L_{s\sigma} + L_m$ and $L_r = L_{r\sigma} + Lm$.

The principal idea behind vector control strategy is to make the control of induction motor similar to that of a dc machine. The field-oriented control is beneficial from the control point of view as the control inputs (V_{s_d}, V_{s_q}) directly affect the current dynamics only (i_{s_d}, i_{s_q})[1]. In this implementation, proportional-integrator (PI) controllers are used for both current and speed control applications[32]. As shown in Figure 9, the output of the PI speed controller is the torque set point reference τ_{ref} for the current controller. The output of the current controller is the voltage in $dq0$ frame, which is then mapped back to abc frame with a pulse width modulation (PWM) inverter in order to include the inverter harmonics in the supply. The three-phase voltage output from the inverter is then fed to induction machine. The normalised speed profiles to the

[1] Here, the subscript s_d and s_q refer to the stator quantities in $dq0$ frame

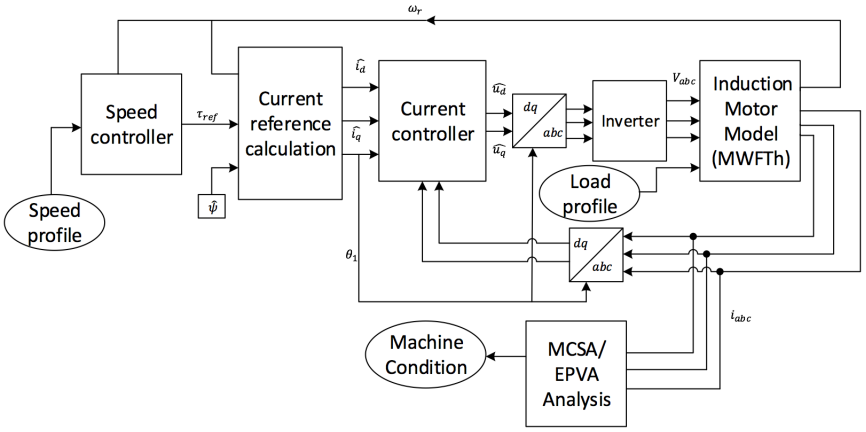

Figure 9. A vector control scheme

speed controller are supplied from the FAST simulations as described in Section 2. The load profiles from the FAST analysis are applied to the induction motor.

Once the controllers are designed and tested with the lumped model, they are simulated in closed-loop with the models incorporating faults, described in Section 3. The stator currents from the fault models are then captured and analysed using FFT. In this way, the effectiveness of current signature based analyses are studied in the pitch system environment.

The data obtained from FAST simulation described in Section 2 is used to simulate the developed closed-loop system. Since the detailed induction motor model is nonlinear, a very low sample time in the order of $1\mu s$ is necessary to run the model accurately. In order to reduce computational burden, the 160 seconds of simulated data is cut into snapshots of 10 seconds each. The corresponding normalised load profile is applied. As the motor current signature analysis assumes fixed supply frequency, regions of relatively steady operation (with speed variations less than 10 rpm) are chosen for evaluation. One such case is presented here, wherein the motor is running steady at 2762 rpm for about 3.5 seconds. The three phase currents stator currents i_s are collected for this period and analysed using standard FFT technique. The mean speed is obtained from the model and the supply frequency is evaluated from the voltage supplied by the controller to be 46.54 Hz. Firstly, the healthy motor is simulated and the current spectrum as well as the dq loci are shown in Figures 10 and 11 respectively.

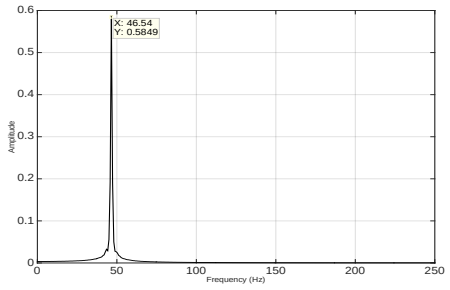

Figure 10. Closed-loop FFT

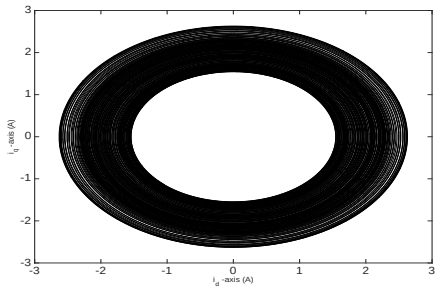

Figure 11. dq-current loci

Further, the AGE fault is simulated with a degree of eccentricity of about 3% variation in airgap similar to the case in open-loop. The results are shown in Figures 12 and 13. It can be seen that although the harmonics as described by equation (18) at the supply frequency are

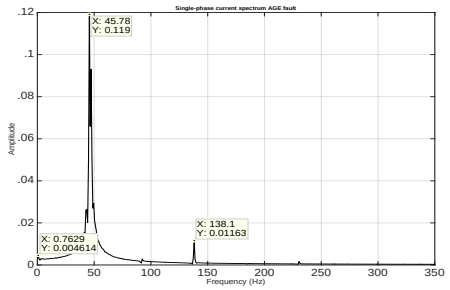

Figure 12. Fault frequencies at f_{AGE_1}

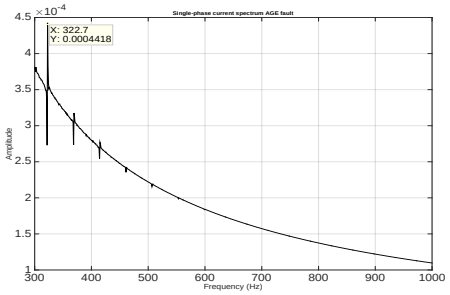

Figure 13. Fault frequencies at f_{AGE_2}

present, the higher frequency harmonics as described by equation (19) are almost invisible. This is due to the fact that the load is significantly varying in this region. The supply frequency of 46.54Hz was filtered from the current signal using a notch filter.

The BRG fault is also similarly visible with about $4\mu m$ variation in the airgap due to outer race crack. The results are shown in Figure 14. It is to be noted that the load variations have shown little effect on MCSA in AGE as well as BRG cases. However, BRB fault was undetectable despite increasing the resistance of the upto 15 rotor bars to 50 times there normal value, as opposed to clear signature with only 2 rotor bars breakage in the open-loop with constant loading. This could be due to the controller in loop as well as the variable loads. The spectrum for BRB fault is shown in Figure 15.

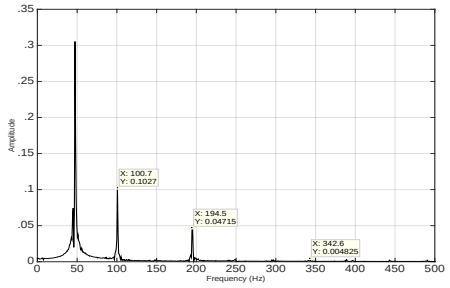

Figure 14. Bearing fault spectrum

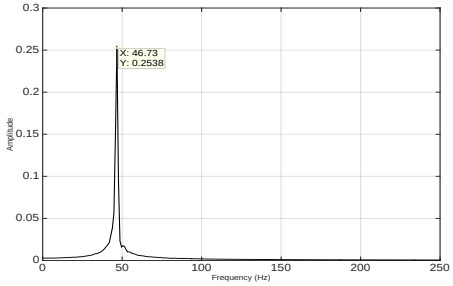

Figure 15. Broken rotor-bar fault spectrum

Finally, the stator turn fault (STF) is tested with 15% windings shorted in the phase A. The single phase current spectrum as well as the dq current loci in faulty condition are depicted in Figures 16 and 17, respectively. It can be noticed that the $3f_s$ frequency for the supply frequency $f_s = 46.54$ Hz is clearly noticeable in the spectrum. The dq loci is also elliptical, due to the presence of the fault as opposed to being circular in the case of healthy machine as shown in Figure 11.

Table 2. Calculated fault frequencies in closed-loop

f_{BRG}(Hz)	f_{BRB}(Hz)	f_{age_1}(Hz)	f_{age_2}(Hz)
101.07	47.36	92.66	783.8
194.15	45.71	0.41	1014.4
341.7		138.7	1106.7
		184.10	1245.9

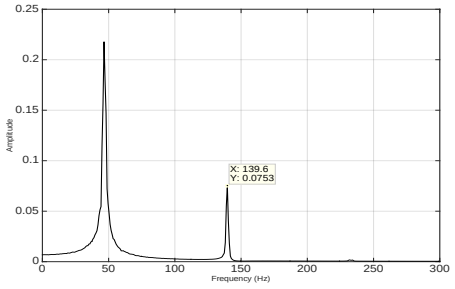

Figure 16. i_d-current spectrum

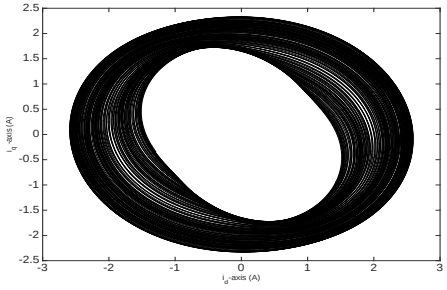

Figure 17. dq-current loci

The fault frequencies in all the fault cases are calculated based on the equations (18-21). These are described in Table 2. These are in good agreement with the results obtained from the simulations.

5. Conclusion

The motor current signature analysis based on FFT is tested in wind turbine pitch system scenario for detecting pitch motor faults. The tests are performed on a detailed model of induction motor, based on modified winding function theory . Each fault condition is modelled capturing the physics of fault and the current signatures are tested. It was noticed that the speed of motor, the duration of operation, fault severity and loading conditions affect the effectiveness of FFT based diagnostics. It has been observed that as long as the speed of the motor is relatively constant and above 65% of the rated speed, even for a short duration, there appears to be good chance in detecting the faults. If the recommended practice to rotate the pitch bearing by a large amplitude periodically (once per day) to ensure even spread of lubrication in pitch bearing[33] is followed, then the assumptions on availability of constant speed operation data may be reasonable. Further, a speed sensor or drive's internal speed measurement can be used as a basis to detect the short windows of constant speed for diagnostics. The diagnostics need not necessarily be continuous and can utilise these short windows of about 100 rotations as demonstrated here. Besides, it is also beneficial to do so as this would require relatively less computational resources and data transfers to maintenance personnel.

The approach presented here has a few challenges to overcome. Firstly, a detailed multi-body model including the gearbox and blade bearing is necessary to adequately estimate the inertia and realistic response times of the pitch system. Besides, pitch rate limits can greatly determine the operational speed and the detection capability of MCSA. Secondly, the inverter is not modelled into the control loop designed here. This was a step taken only to reduce further complexity of the model. The effect of inverter harmonics on the reliability of diagnostics needs

to be investigated.
The stator winding faults, bearing faults and air gap eccentricity faults appear detectable in relatively steady operating speeds, despite load variation within very short time windows, using conventional MCSA. However, if the speed is inconstant, and very quick start-stop operations are to be considered, then advanced methods based on time-frequency analysis such as wavelets [34] or other techniques such as the so called Vienna monitoring method [35] are to be evaluated. Further, if the MCSA technique is found to be reliable, it is well suited for farm-level implementation of pitch system diagnostics for two reasons. One, it can be integrated into the controller as current and speed measurements are usually included in motor drives. If this is not possible, it only requires installation of current sensors, which are inexpensive and clip on to the supply cables with minimal modifications to the existing setup. And two, FFT based methods are advantageous as they require relatively less computational power. Therefore, this study appears to be a promising start for further analysis and development of reliable diagnostics of pitch motors.

Acknowledgements
This work has been funded by Norwegian Centre for Offshore Wind Energy (NORCOWE) under Grant 193821/S60 from Research Council of Norway (RCN). NORCOWE is a consortium with partners from industry and science, hosted by Christian Michelsen Research.

Appendix-A
The healthy motor parameters [21] used for modelling the induction motor are detailed here:

Table 3. Motor parameters used for simulation

Parameter	Units	Values
rotor (effective) axial length l	m	120×10^{-3}
rotor radius r	m	70×10^{-3}
airgap length g	m	0.28×10^{-3}
number of stator turns N_t		156
number of rotor bars N_r		28
rotor inertia J	kg/m^2	0.002
number of poles p		2
stator resistance r_s	Ω	1.5
stator leakage inductance L_{ls}	$\mathbb{H}$	7×10^{-3}
rotor bar resistance r_b	Ω	96×10^{-6}
rotor bar leakage inductance L_b	$\mathbb{H}$	0.28×10^{-6}
rotor end ring resistance r_e	Ω	5×10^{-6}
rotor end ring inductance L_e	$\mathbb{H}$	0.036×10^{-6}

References

[1] Kandukuri S T, Robbersmyr K G and Karimi H R 2016 *The International Journal of Advanced Manufacturing Technology* **83** 1557–67
[2] Crabtree C J, Zappalá D and Tavner P J 2014 Survey of commercially available condition monitoring systems for wind turbines. Technical report SUPERGEN, Durham University URL `http://dro.dur.ac.uk/12497/`
[3] 2006 Doing business with wind turbine manufcaturers: becoming part of their supply chain Technical report Douglas-Westwood Limited & BVG Associates
[4] Gayo J B 2011 Final Publishable Summary of Results of Project ReliaWind Technical report FP7-Energy-2007-1-RTD
[5] Bossanyi E A 2003 *Wind Energy* **6** 229–44
[6] Odgaard P F, Stoustrup J and Kinnaert M 2013 *IEEE Transactions on Control Systems Technology* **21** 1168–82
[7] Yin S, Wang G and Karimi H 2014 *Mechatronics* **24** 298–306
[8] Jonkman J, Butterfield S, Musial W and Scott G 2009 Definition of a 5-mw reference wind turbine for offshore system development Technical Report NREL/TP-500-38060 National Renewable Energy Laboratory

[9] Jonkman B 2009 Turbsim user's guide: Version 1.50 Tech. Rep. NREL/TP-500-46198 National Renewable Energy Laboratory
[10] LM Wind Power 2015 URL `http://www.lmwindpower.com/Rotor-Blades/Products/Blade-Summary`
[11] Rothe Erde Thyssen Krupp Dortmund, Germany 2007 *Slewing Bearings (Catalogue)*
[12] Townsend D, Allen C and Zaretsky E 1973 Study of ball bearing torque under elastohydrodynamic lubrication Technical Memorandum NASA TM X-68271 National Aeronautics and Space Administration
[13] Brevini Power Transmission S.p.A. Reggio Emilia, Italy *Slewing Drives (Catalogue)*
[14] Bakka T and Karimi H 2013 *Journal of the Franklin Institute* **350** 2244–60
[15] 2005 *IEC 61400-1 Wind turbine generator systems - Part 1: Design requirements, III Edition* (International Electrotechnical Commission (IEC))
[16] Albrecht P, Appiarius J, McCoy R, Owen E and Sharma D 1986 *IEEE Transactions on Energy Conversion* **EC-1** 39–46
[17] Nandi S, Toliyat H A and Xiaodong L 2005 *Energy Conversion, IEEE Transactions on* **20** 719–29
[18] Thomson W and Fenger M 2003 Case histories of current signature analysis to detect faults in induction motor drives *IEEE International Electric Machines and Drives Conference, 2003. IEMDC'03.* vol 3 (IEEE) pp 1459–65
[19] Krause P and Thomas C 1965 *IEEE Transactions on Power Apparatus and Systems* **84** 1038–53
[20] Lipo T A 2012 *Analysis of Synchronous Machines* 2nd ed (Taylor & Francis Group, Florida, US: CRC Press)
[21] Ibrahim A K, Marei M I, El-Gohary H S and Shehata S A M 2010 Modeling of induction motor based on winding function theory to study motor under stator/rotor internal faults *Proceedings of the 14th International Middle East Power Systems Conference (MEPCON'10)* pp 494–500
[22] Toliyat H, Nandi S, Choi S and Meshgin-Kelk H 2013 *Electric Machines Modeling Condition Monitoring and Fault Diagnosis* (Taylor & Francis Group, LLC, Boca Raton, Florida, USA.: CRC Press)
[23] Nandi S, Bharadwaj R and Toliyat H 2002 *IEEE Transactions on Energy Conversion* **17** 392–99
[24] Blodt M, Granjon P, Raison B and Rostaing G 2008 *IEEE Transactions on Industrial Electronics* **55** 1813–22
[25] Munoz A R and Lipo T A 1999 *IEEE Transactions on Industry Applications* **35** 1332–40
[26] Sahraoui M, Ghoggal A, Zouzou S and Benbouzid M 2008 *Simulation Modelling Practice and Theory* **16** 1503–13
[27] Nandi S, Ahmed S and Toliyat H 2001 *IEEE Transactions on Energy Conversion* **16** 253–60
[28] Schiltz R 1990 *Journal of Sound and VIbration* **24** 16–19
[29] Thomson W T and Fenger M 2001 *IEEE Industry Applications Magazine* **7** 26–34 ISSN 10772618
[30] Cruz S and Cardoso A 2001 *IEEE Transactions on Industry Applications* **37** 1227–33
[31] Marques Cardoso A, Cruz S and Fonseca D 1999 *IEEE Transactions on Energy Conversion* **14** 595–98
[32] Harnefors L 2003 *Control of Variable-Speed Drives* (Mälarden University, Sweden)
[33] Harris T, Rumbarger J H and Butterfield C P 2009 Wind Turbine Design Guideline DG03 : Yaw and Pitch Rolling Bearing Life Technical Report NREL/TP-500-42362 National Renewable Energy Laboratory (NREL)
[34] Teotrakool K, Devaney M J and Eren L 2006 Adjustable Speed Drive Bearing Fault Detection via Wavelet Packet Decomposition *IEEE Instrumentation and Measurement Technology Conference Proceedings* (IEEE) pp 22–25
[35] Wieser R, Schagginger M, Kral C and Pirker F 1998 The integration of machine fault detection into an indirect field oriented induction machine drive control scheme-the Vienna Monitoring Method *IEEE Industry Applications Conference. Thirty-Third IAS Annual Meeting* vol 1 pp 278–85